Simulating temporal evolution of pressure in two-phase flow in porous media

Eyvind Aker* and Knut Jørgen Måløy
Department of Physics, University of Oslo, N-0316 Oslo, Norway

Alex Hansen
Department of Physics, Norwegian University of Science and Technology, N-7034 Trondheim, Norway
(Received 17 November 1997; revised manuscript received 17 April 1998)

We have simulated the temporal evolution of pressure due to capillary and viscous forces in two-phase drainage in porous media. We analyze our result in light of macroscopic flow equations for two-phase flow. We also investigate the effect of the trapped clusters on the pressure evolution and on the effective permeability of the system. We find that the capillary forces play an important role during the displacements for both fast and slow injection rates and both when the invading fluid is more or less viscous than the defending fluid. The simulations are based on a network simulator modeling two-phase drainage displacements on a two-dimensional lattice of tubes. [S1063-651X(98)08208-7]

PACS number(s): 47.55.Mh, 07.05.Tp, 05.40.+j

I. INTRODUCTION

Fluid flow in porous media such as sand, soil, and fractured rock is an important process in nature and has a huge number of practical applications in engineering. It is most often mentioned in oil recovery and hydrology. Fluid flow in porous media has also been of great interest in modern physics. In particular, the different structures of the interface between the fluids in two-phase displacements have been extensively studied. Despite this attention there are still many open questions concerning fluid flow in porous media.

In this paper we report on simulations of the temporal evolution of pressure during two-phase drainage in a model porous medium, consisting of a two-dimensional lattice of tubes. The network model has been developed to measure the time dependence of different physical properties and to study the dynamics of the fluid movements. Especially, we focus on the dynamics of the temporal evolution of the pressure due to capillary and viscous forces and the time dependence of the front between the two liquids. The discussion is restricted to drainage displacement, i.e., the process where a nonwetting fluid displaces a wetting fluid in a porous medium.

During the last two decades an interplay between experimental results and numerical simulations has improved the understanding of the displacement process. It has been shown that the different structures observed when changing the physical parameters of the fluids like viscosity contrast, wettability, interfacial tension, and displacement rate [1–6] divide into three flow regimes. These three major regimes are referred to as viscous fingering [1,2], stable displacement [3], and capillary fingering [7]. There exist statistical models such as diffusion-limited aggregation (DLA) [8], anti-DLA [9], and invasion percolation [10] that reproduce the basic domains in viscous fingering, stable displacement, and capillary fingering, respectively. However, these models do not contain any physical time for the front evolution and they cannot describe the crossover between the different flow regimes.

Much effort has gone into making better models whose properties are closer to those of real porous media. This has resulted in several network simulators, modeling fluid flow on a lattice of pores and throats [2,3,11–20]. Most of the network models have been used to obtain new information on the different flow regimes and to study the statistical properties of the displacement structures. Others have been used to calculate macroscopic properties like fluid saturations and relative permeabilities and compare them with corresponding experimental data. In Ref. [20] a network model simulating the pressure buildup during drainage is presented. That work shows that many questions remain to be answered about how pressure buildup is linked to the displacement structure. Here we present a systematic discussion of the interplay between capillary and viscous forces at various injection rates. The results are based on a network simulator that properly simulates the dynamics of capillary pressure variations as well as the viscous pressure buildup.

We have simulated the temporal evolution of the pressure in all three regimes of interest: viscous fingering, stable displacement, and capillary fingering. The injection rate in the displacements has been systematically varied and we have analyzed the behavior of the pressure in the crossover between the three regimes. Moreover, we discuss what effect trapped clusters have on the evolution of the pressure in the system and we relate the data to macroscopic flow equations. We find the surprising result that capillary forces play an important role in two-phase flow at both high and low injection rates.

The paper is organized as follows. In Sec. II we present the network model, in Sec. III we present and discuss the simulation results, and in Sec. IV we draw some conclusions.

II. NETWORK MODEL

The network model has been presented in [21] and we will restrict ourselves to a short sketch here.

*Also at Norwegian University of Science and Technology, N-7034 Trondheim, Norway.

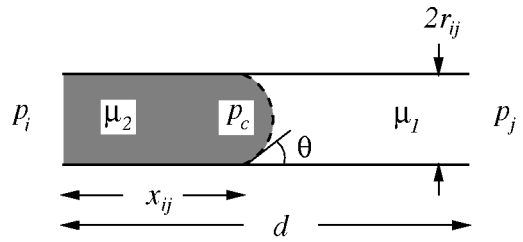

FIG. 1. Flow in a tube containing a meniscus.

A. Geometry and boundary conditions

The porous medium is represented by a square lattice of tubes oriented at 45°. At each node four tubes meet and there is no volume assigned to the nodes: the tubes represent the volume of both pores and throats. The tubes are cylindrical with length d. Each tube is assigned an average radius r which is chosen at random in the interval $[\lambda_1 d, \lambda_2 d]$, where $0 \leqslant \lambda_1 < \lambda_2 \leqslant 1$. The randomness of the radii represents the disorder in the model.

The liquids flow from the bottom to the top of the lattice and we implement periodic boundary conditions in the horizontal direction. The pressure difference between the bottom row and the top row defines the pressure across the lattice. Gravity effects are neglected, and consequently we consider horizontal flow in a two-dimensional network of tubes.

B. Fluid flow through the network

Initially, the system is filled with a defending fluid with viscosity μ_1. The invading fluid with viscosity μ_2 is injected along the bottom row with a constant injection rate. We model drainage, i.e., the invading fluid is nonwetting and the defending fluid is wetting. Furthermore, we assume that the fluids are incompressible and immiscible. Consequently, the volume flux is conserved everywhere in the lattice and a well-defined interface develops between the two phases.

The capillary pressure p_c due to the interface between the nonwetting and wetting fluid inside a tube (a meniscus) is given by the Young-Laplace law

$$p_c = \frac{2\gamma}{r} \cos\,\theta. \tag{1}$$

Here r is the radius of the tube, γ is the interfacial tension, and θ denotes the wetting angle between the nonwetting and wetting phases. θ is in the interval $(0, \pi/2)$ for drainage displacements.

With respect to the capillary pressure we assume that the tubes are hourglass shaped with effective radii following a smooth function. Thus the capillary pressure becomes a function of the position of the meniscus in the tube and we assume that the Young-Laplace law (1) takes the form

$$p_c = \frac{2\gamma}{r}[1 - \cos(2\pi\hat{x})]. \tag{2}$$

Here $\hat{x}$ is the dimensionless value of the meniscus's position in the tube ($0 \leqslant \hat{x} \leqslant 1$), and $\theta = 0$ (perfect wetting). From Eq. (2) $p_c = 0$ at the ends of the tube while p_c approaches its maximum of $4\gamma/r$ in the middle of the tube.

The volume flux q_{ij} through a tube from the ith to the jth node in the lattice (Fig. 1) is found from the Washburn equation for capillary flow [22]. As an approximation we treat the tubes as if they were cylindrical and obtain

$$q_{ij} = -\frac{\pi r_{ij}^2 k_{ij}}{\mu_{\text{eff}}} \frac{1}{d}(\Delta p_{ij} - \tilde{p}_c). \tag{3}$$

Here k_{ij} is the permeability of the tube given by $k_{ij} = r_{ij}^2/8$ where r_{ij} is the average radius of the tube. $\Delta p_{ij} = p_j - p_i$ is the pressure difference between the ith and jth node. A tube partially filled with both liquids is allowed to contain either one or two menisci. If the tube contains one meniscus, the meniscus can point to the right as in Fig. 1 or to the left. A tube containing two menisci can have a trapped wetting (nonwetting) blob between sections of nonwetting (wetting) fluid. The effective viscosity of the tubes, denoted as μ_{eff} in Eq. (3), becomes a sum of the amount of each fluid multiplied by their respective viscosities. The total capillary pressure, $\tilde{p}_c$ in Eq. (3), is the sum of the capillary pressures of the menisci that are inside the tube. The absolute value of the capillary pressure of each meniscus is given by Eq. (2), while its sign depends on whether the meniscus points to the right or to the left. Practically, the wetting angle of a meniscus and thereby its capillary pressure may generally be different depending on whether the meniscus retires from or invades the tube. However, this effect is neglected in the present model.

In the simple case where the tube only contains one meniscus (Fig. 1) $\mu_{\text{eff}} = \mu_2 \hat{x}_{ij} + \mu_1(1 - \hat{x}_{ij})$ and $\tilde{p}_c = p_c$. For a tube without menisci $\tilde{p}_c = 0$, and Eq. (3) reduces to that describing Hagen-Poiseuille flow with $\mu_{\text{eff}} = \mu_1$ or μ_2.

C. Determining the flow field

There is no volume assigned to the nodes giving conservation of volume flux at each node

$$\sum_j q_{ij} = 0. \tag{4}$$

The summation on j runs over the nearest neighbor nodes to the ith node while i runs over all nodes that do not belong to the top or bottom rows, that is, the internal nodes.

Equations (3) and (4) constitute a set of linear equations which are to be solved for the nodal pressures p_j with the constraint that the pressures at the nodes belonging to the upper and lower rows are kept fixed. The set of equations is solved by using the conjugate gradient method [23].

We want to study the dynamics of the pressure fluctuations at constant displacement rate. Therefore we need to find the pressure across the lattice for a desired injection rate and then use that pressure to solve fluid flow through the network. For two-phase displacement the pressure across the lattice ΔP is related to the injection rate Q through the equation

$$Q = A\Delta P + B. \tag{5}$$

Here A and B are parameters depending on the geometry of the medium and the current configuration of the liquids. The first part of Eq. (5) is simply Darcy's law for one-phase flow,

while the last part B results from the capillary pressure between the two phases. As long as the menisci do not move B is constant.

The pressure Δp_{ij} across each tube can be related to the pressure across the lattice ΔP. All the equations calculating the fluid flow in the system, have the functional form $f(x) = ax + b$. As a consequence Δp_{ij} becomes a function of ΔP,

$$\Delta p_{ij} = \Gamma_{ij} \Delta P + \Pi_{ij} . \tag{6}$$

Γ_{ij} is a dimensionless quantity depending on the mobilities (k/μ_{eff}) of the tubes and Π_{ij} is a function of the capillary pressures of the menisci inside the tubes. If no menisci in the network are present Π_{ij} is zero. Equation (6) can easily be deduced for two cylindrical tubes with different radii connected in series.

By inserting Eq. (6) into Eq. (3) we obtain after some algebra a relation between the local flow rate q_{ij} and the pressure ΔP across the network,

$$q_{ij} = \tilde{a}_{ij} \Delta P + \tilde{b}_{ij} . \tag{7}$$

The parameter $\tilde{a}_{ij}$ is proportional to Γ_{ij} and the mobility $(k_{ij}/\mu_{\text{eff}})$ of tube ij. $\tilde{b}_{ij}$ contains the capillary pressures of the menisci.

The solution due to a constant injection rate can now be summarized into the following steps.

(1) We first find the nodal pressures for two different pressures $\Delta P'$ and $\Delta P''$ applied across the lattice.

(2) From the two solutions of the nodal pressures the corresponding injection rates Q' and Q'' and the local flow rate q'_{ij} and q''_{ij} are calculated.

(3) A and B is calculated by solving the two equations obtained when inserting $\Delta P'$, Q', $\Delta P''$, and Q'' into Eq. (5).

(4) The pressure ΔP across the lattice for the desired Q is then calculated by using Eq. (5).

(5) This ΔP is inserted in Eq. (7) to get the local flow q_{ij}. Note that parameters $\tilde{a}_{ij}$ and $\tilde{b}_{ij}$ are already known from step 2 by solving the two equations obtained by inserting q'_{ij}, $\Delta P'$, q''_{ij}, and $\Delta P''$ into Eq. (7).

D. Moving the menisci

A time step Δt is chosen such that every meniscus is allowed to travel at most a maximum step length $\Delta x_{\max}$ during that time step. Numerical simulations show that in order to calculate the effect of capillary pressure changes when a meniscus travels through a tube, $\Delta x_{\max}$ should be of order $0.1d$ (d is the tube length). Thus to let a meniscus pass one tube at least ten iterations should be made. Every simulation presented in this paper was performed with constant $\Delta x_{\max} \leqslant 0.1d$.

In each time step we check whether or not a meniscus crosses a node. If this happens, the time step is redefined such that this meniscus stops at the end of the tube. A meniscus reaching the end of a tube is moved into the neighbor tubes according to well-defined rules [20]. These rules take care of the different fluid arrangements that can appear around the node. Basically, the nonwetting fluid can either invade into or retreat from the neighbor tubes as shown in Figs. 2(a) and 2(b), respectively. In Fig. 2(a) the nonwetting fluid approaches the node from below (drainage). When the meniscus has reached the end of the tube (position 1), it is removed and three new menisci are created at position δ in the neighbor tubes (position 2). The distance δ is about 1–5 % of the tube length d. The small distance δ avoids that the menisci created at positions 2 immediately disappear and move back to the initial position 1 in tubes where the flow direction is opposite to the direction of the invading fluid. The total time lapse is adjusted to compensate the instantaneous change in local volume of the fluids when the menisci move a distance δ and such that the total volume of the fluids always is conserved.

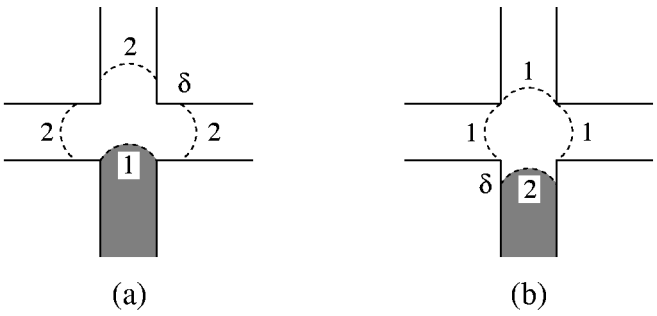

FIG. 2. Motion of the menisci at the nodes. (a) The nonwetting fluid (shaded) reaches the end of the tube (position 1) and is moved a distance δ into the neighbor tubes (position 2). (b) The wetting fluid (white) reaches the end of the tubes (position 1) and the nonwetting fluid (shaded) retreats to position 2. To conserve the volume of the fluids an appropriate time lapse is taken into account due to the small movement δ in (a) and (b).

Figure 2(b) shows the opposite case when the nonwetting fluid retreats into a single tube (imbibition). As Fig. 2(b) shows, the properties of imbibition should not be neglected as long as the menisci can travel in both directions. Our approximation in Fig. 2(b) cannot handle important properties found in imbibition such as film flow and snap off [5,24]. However, in drainage which is what we are focusing on, arrangement (b) will appear rarely compared to (a). For that reason, any further description of imbibition than the one presented in Fig. 2(b) does not seem necessary—at least at this stage.

Summarized, the procedure for each time step Δt follows.

(1) The nodal pressures p_j are determined.

(2) The p_j's are related to the desired injection rate Q from Eqs. (5) and (7).

(3) The local flow rate in each tube is computed by using Eq. (3).

(4) The local flow rates are used to calculate the time step Δt such that only one meniscus reaches the end of a tube or travels at most the step length $\Delta x_{\max}$ during that time step.

(5) The menisci are updated according to Δt. The total time lapse is recorded before the whole procedure is repeated for the new fluid configuration.

III. SIMULATIONS

In two-phase fluid displacement there are mainly three types of forces: viscous forces in the invading fluid, viscous forces in the defending fluid, and capillary forces due to the interface between them. This leads to two dimensionless

numbers that characterize the flow: the capillary number C_a and the viscosity ratio M.

The capillary number describes the competition between capillary and viscous forces. It is defined as

$$C_a = \frac{Q\mu}{\Sigma\gamma}, \tag{8}$$

where Q (cm^2/s) denotes the injection rate, μ (Poise) is the maximum viscosity of the two fluids, Σ (cm^2) is the cross section of the inlet, and γ (dyn/cm) is the interfacial tension between the two phases. Σ is calculated by taking the product of the length of the inlet and the mean thickness of the lattice due to the average radius of the tubes.

M defines the ratio of the viscosities of the two fluids and is given by the invading viscosity μ_2 divided by the defending viscosity μ_1:

$$M = \frac{\mu_2}{\mu_1}. \tag{9}$$

In the simulations the pressure across the lattice ΔP is given by Eq. (5) as

$$\Delta P = \frac{Q}{A} - \frac{B}{A} = \frac{Q}{A} + P_{cg}. \tag{10}$$

Since B is due to the capillary pressure of the menisci, we define $-B/A$ as the global capillary pressure of the system, P_{cg}. P_{cg} includes the menisci surrounding the trapped clusters of defending fluid (cluster menisci) as well as the menisci belonging to the front between the invading and defending fluid (front menisci).

In addition to P_{cg} we calculate P_{cf}, the capillary pressure averaged along the front. P_{cf} consists only of the capillary pressures due to the front menisci and we define it as

$$P_{cf} = \frac{1}{N}\sum_{\alpha=1}^{N} |p_c^\alpha|. \tag{11}$$

Here the index α addresses the tubes in the lattice and in the summation α runs over all tubes containing a meniscus that belong to the front. N is the number of such tubes. p_c^α is the capillary pressure of the front meniscus in tube α. The tubes containing a front meniscus or belonging to trapped clusters of defending fluid are identified by running a Hoshen-Kopelman algorithm [25] on the lattice.

For every simulation we have calculated ΔP and P_{cg} as functions of time. For some of the simulations we have also computed the average capillary pressure P_{cf} along the front and analyzed the behavior of A in Eq. (5). As will be discussed below, ΔP, P_{cg}, and P_{cf} are strongly correlated and A seems to obey surprisingly simple relations.

We have performed drainage simulations in each of the regimes of interest: viscous fingering, stable displacement, and capillary fingering with $M = 1.0\times10^{-3}$, 1.0, and 1.0×10^{2}, respectively. The injection rate was systematically varied for each of the viscosity ratios. Figure 3 shows a visualization of three simulations one in each of the regimes viscous fingering, stable displacement, and capillary fingering.

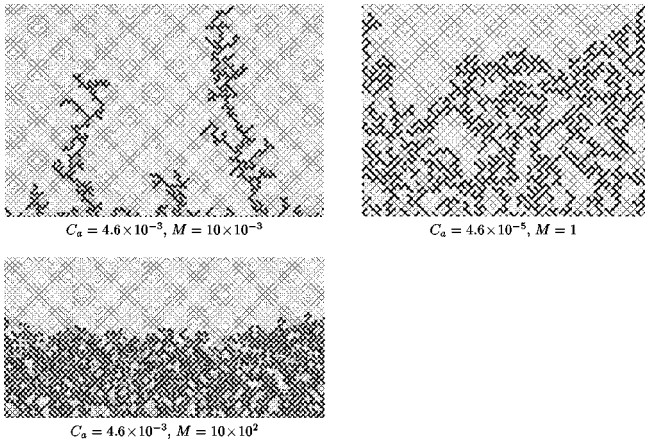

FIG. 3. Displacement structure of three simulations, one in each of the regimes viscous fingering (top left), capillary fingering (top right), and stable displacement (bottom left). The patterns show the characteristic features of the three regimes. The invading, nonwetting fluid (black) displaces the defending, wetting fluid (gray) from below. The size of the lattice was 60×80 nodes for viscous fingering, 40×60 nodes for capillary finger, and 60×60 nodes for stable displacement.

At high injection rate with $M<1$ we approach the regime of viscous fingering. In viscous fingering the principal force is due to the viscous forces in the defending fluid and the pattern formation in Fig. 3 for $C_a = 4.6\times10^{-3}$, $M = 10\times10^{-3}$, shows that the invading fluid creates typical fingers into the defending fluid.

Stable displacements are obtained at high injection rate with $M>1$. Then the fluid movements are dominated by the viscous forces in the invading liquid and the pressure gradient in the invading phase is found to stabilize the front. A typical compact pattern with an almost flat front between the nonwetting and wetting fluid is generated as shown in Fig. 3 for $C_a = 4.6\times10^{-3}$, $M = 10\times10^{2}$. The stabilized front introduces a length scale in the system for large times. This length scale is identified as the saturation width w_s of the front [26]. The width of the front w is defined as the standard deviation of the distances between all the front tubes and the average position of the front.

At sufficient low injection rate we approach the regime of capillary fingering independent of the viscosity ratio. In capillary fingering the displacement is so slow that the viscous forces are negligible, with the consequence that the main force is the capillary one between the two fluids. Only the strength of the threshold pressure in a given tube decides whether the invading fluid moves across that tube or not. The invading fluid creates a rough front with trapped clusters that appear at all scales between the tube length and the maximum width of the front (Fig. 3 for $C_a = 4.6\times10^{-5}$, $M = 1$).

The simulations were performed with parameters as close as possible to experiments performed in [25]. The length d of all tubes in the lattices was set equal to 1 mm and the radii r of the tubes were chosen randomly in the interval $0.05d \leqslant r \leqslant d$. The interfacial tension was set to $\gamma = 30$ dyn/cm and the viscosities of the defending and the invading fluids were varied between 0.01 P ($\simeq$ water) and 10 P ($\simeq$ glycerol).

A. Viscosity ratio, $M<1$

We have performed a series of simulations with constant viscosity ratio $M = 1.0\times10^{-3}$, going from high to low injec-

TABLE I. Lattice size and the values for the injection rate and the capillary number when $M=1.0\times10^{-3}$.

Size (nodes)	Injection rat (cm^3/min)	C_a
60×80	1.5	4.6×10^{-3}
25×35	1.4	1.1×10^{-2}
25×35	0.98	7.1×10^{-3}
25×35	0.62	4.7×10^{-3}
25×35	0.50	3.6×10^{-3}
25×35	0.099	7.2×10^{-4}
25×35	0.049	3.5×10^{-4}

tion rate. The injection rates and the capillary numbers used are listed in Table I. At high capillary number we are in the regime of viscous fingering, however, when the capillary number is reduced we approach the regime of capillary fingering. To save computation time, most of the simulations were performed on a lattice of 25×35 nodes. One was performed on a lattice of 60×80 nodes whose resulting structure is shown in Fig. 3.

Figure 4 shows the pressure evolutions of the simulation at $C_a=4.6\times10^{-3}$ in the regime of viscous fingering. The pressure across the lattice, ΔP (a), decreases as the less viscous fluid invades the system. The slope of the average decreasing pressure function is nontrivial and results from the fractal development of the fingers. The global capillary pressure P_{cg} (b) fluctuates around a mean value of about 1×10^3 dyn/cm^2. The fluctuation is strongly correlated in both time and amplitude to the noise in ΔP. This is clarified by plotting the difference $\Delta P-P_{cg}$ (c) which becomes a smooth curve. As will be discussed below, the fluctuations correspond to variations in capillary pressure as menisci invade into or retreat from tubes.

We have calculated P_{cf} for every simulation performed on the lattices of 25×35 nodes. The result for four of the simulations is shown in Fig. 5 together with the global capillary pressure P_{cg}. The pressures in Fig. 5 are normalized by dividing them with the average threshold pressure of the tubes. The average threshold pressure is defined as $2\gamma/\langle r\rangle$ where $\langle r\rangle$ is the mean radius of the tubes. The mean threshold pressure is about 1.1×10^3 dyn/cm^2 in all simulations, since the radii of the tubes always are chosen randomly in the interval [0.05,1.0] mm. Note that in Fig. 5, P_{cg} has been subtracted by 1000 dyn/cm^2 before it was normalized. This avoids the plotted pressure functions to overlap at low capillary numbers.

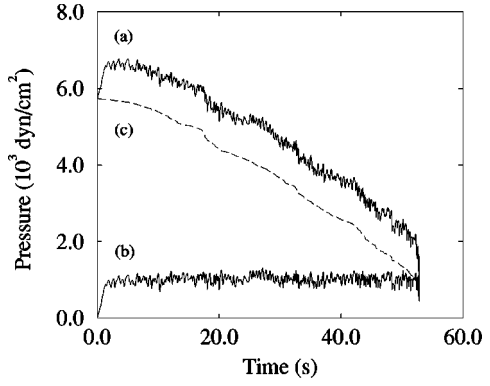

FIG. 4. ΔP (a), P_{cg} (b), and $\Delta P-P_{cg}$ (c) plotted as a function of time. $C_a=4.6\times10^{-3}$ and $M=1.0\times10^{-3}$.

Figure 5 shows that the fluctuations of P_{cf} (a) are correlated in time to the fluctuations of P_{cg} (b). For the simulations at $C_a>3.5\times10^{-4}$ the amplitude of the fluctuations in P_{cf} decreases with injection time. For high injection rates the normalized P_{cf} is found to approach 1, which is the mean threshold pressure. Due to the less viscous defending fluid the pressure gradient at high injection rates is largest at the fingertips closest to the upper boundary of the lattice. The menisci in the uppermost fingertips will therefore more likely continue to invade the next tubes compared to the menisci lying behind it, as the latter are shielded by the moving fingertips causing their capillary pressures to be less than the threshold pressures needed to invade the tubes. The menisci of the moving fingertips give a time dependent contribution to P_{cf} as they travel through the tubes they invade. This is in contrast to the menisci lying behind, that get stuck due to the low pressure gradient, and only contribute a constant value to P_{cf}. Thus for sufficient large systems the fluctuations in P_{cf} will eventually die off when the number of stuck front menisci becomes much larger than the menisci of the moving fingertips.

At lowest $C_a=3.5\times10^{-4}$ we approach the regime of capillary fingering. In slow capillary fingering, the viscous pressure gradient vanishes causing the capillary pressures of all menisci to be equal to the pressure between the fluids as long as all menisci are stable. Thus the calculated pressure reduces to that describing the capillary fluctuations along the front and $P_{cg}\simeq P_{cf}$ as observed.

We note, however, that the fluctuations in P_{cg} survive at large times even at high injection rates. In Fig. 6 we have plotted P_{cg} (a) for $C_a=1.1\times10^{-2}$ together with the capillary pressure of the meniscus which is located in the tube that always has the largest flow velocity (b). According to the higher pressure gradient at the fingertips we expect that the meniscus with highest flow velocity usually belongs to one of the moving fingertips. From Fig. 6 we conclude that the capillary variations in P_{cg} correspond to the moving menisci. Unfortunately, the present data and statistics are too poor to make it possible to draw any further quantitative conclusions.

B. Viscosity ratio, $M>1$

We have run seven simulations with $M=1.0\times10^2$ spread between high and low capillary number, see Table II. The series of simulations were performed on lattices of size between 25×35 and 60×60 nodes. The simulations at high capillary numbers are in the regime of stable displacement while those at low capillary numbers approach the regime of capillary fingering. To save computation time the simulations performed on the lattices of 40×40 and 60×60 nodes were stopped at some time after the width of the front had stabilized. The other simulations were run until the invading fluid reached the outlet.

The pressure across the lattice ΔP, the global capillary pressure P_{cg}, and $1/A$ were calculated for all simulations. The results for low, intermediate, and high capillary numbers

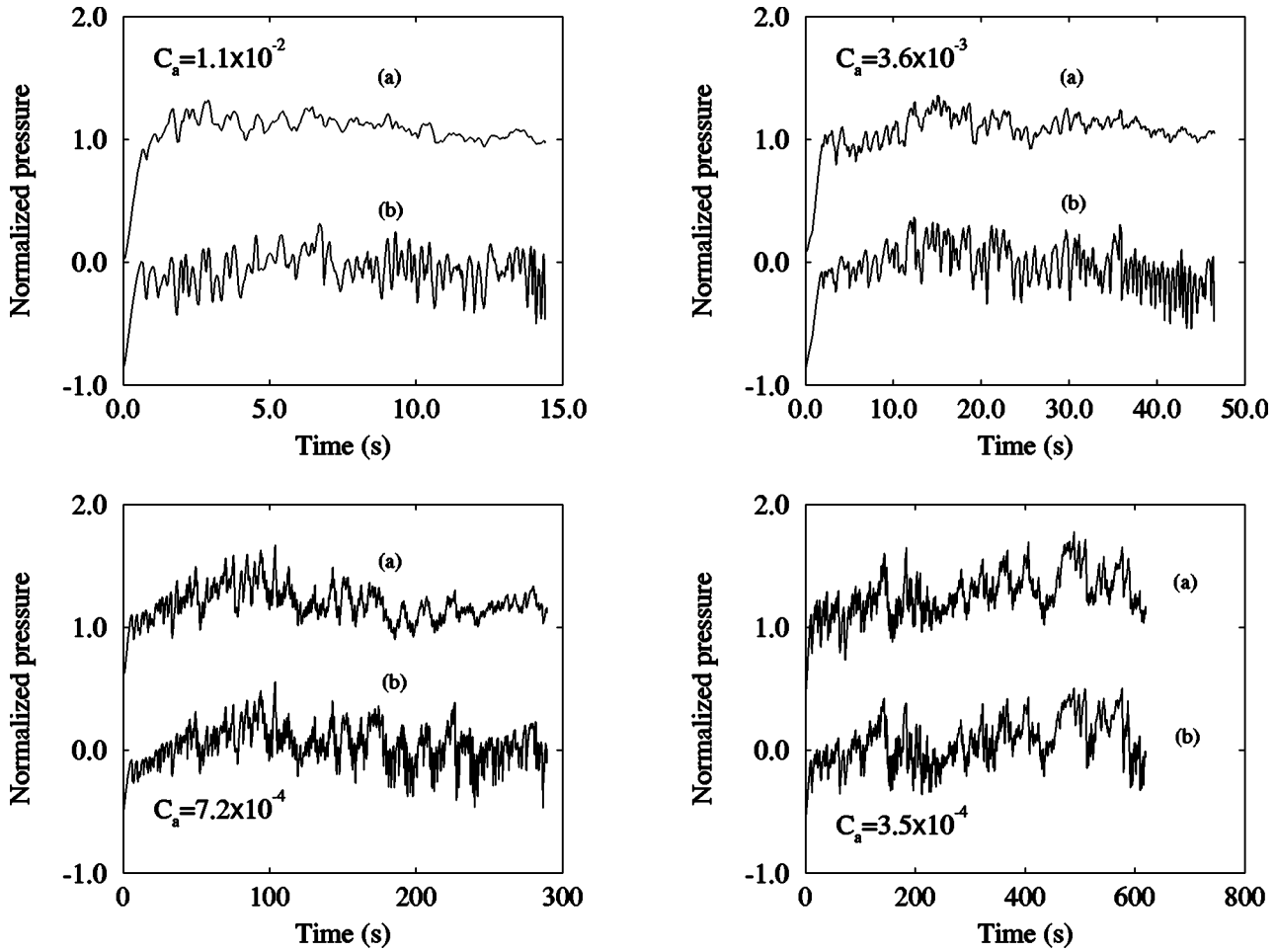

FIG. 5. P_{cf} (a) and P_{cg} (b) at four different capillary numbers for the simulations with $M=1.0\times10^{-3}$ at lattice size 25×35 nodes. The pressures are normalized using the average threshold pressure of the tubes. Note that P_{cg} has been subtracted by 1000 dyn/cm^2 before it was normalized to avoid overlap between the two curves at low capillary numbers.

are shown in Fig. 7. In the figure we have plotted the dimensionless quantity A_0/A instead of $1/A$ where A_0 is equal to the proportionality factor between Q and ΔP when only the defending fluid flows through the lattice, i.e., $A_0=\Sigma K/\mu_1 L$. K denotes the absolute permeability of the lattice and L is the length of the system.

We note that the pressures in Fig. 7 evolve quite differently compared to the pressures in Figs. 4 and 5. ΔP (a) and P_{cg} (b) are both found to increase as the more viscous fluid is injected into the system and the average slope depends very much on the injection rate. To explain this behavior we have to discuss the effect of the trapped cluster of the defending fluid left behind the front. In stable displacement the driving pressure gradient lies between the inlet and the front causing a pressure drop between the top and the bottom of the trapped clusters (viscous drag). At moderate injection rates where the clusters stay in place and keep their shapes, the forces due to the viscous pressure drop must be balanced by capillary forces acting on the cluster menisci. The sum of

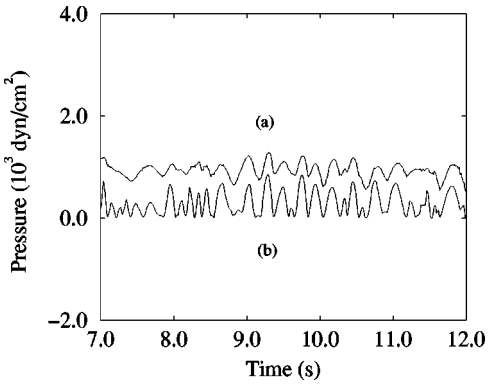

FIG. 6. P_{cg} (a) and the capillary pressure of the meniscus traveling with the highest velocity (b) at $C_a=1.1\times10^{-2}$ and $M=1.0\times10^{-3}$ in the time interval between 7.0 and 12.0 s.

TABLE II. Lattice size and the values for the injection rate and the capillary number when $M=1.0\times10^{2}$.

Size (nodes)	Injection rate (cm^3/min)	C_a
60×60	1.5	4.6×10^{-3}
40×40	1.0	4.6×10^{-3}
25×35	2.5	1.8×10^{-2}
25×35	1.3	9.5×10^{-3}
25×35	0.57	4.2×10^{-3}
25×35	0.29	2.2×10^{-3}
25×35	0.10	7.5×10^{-4}

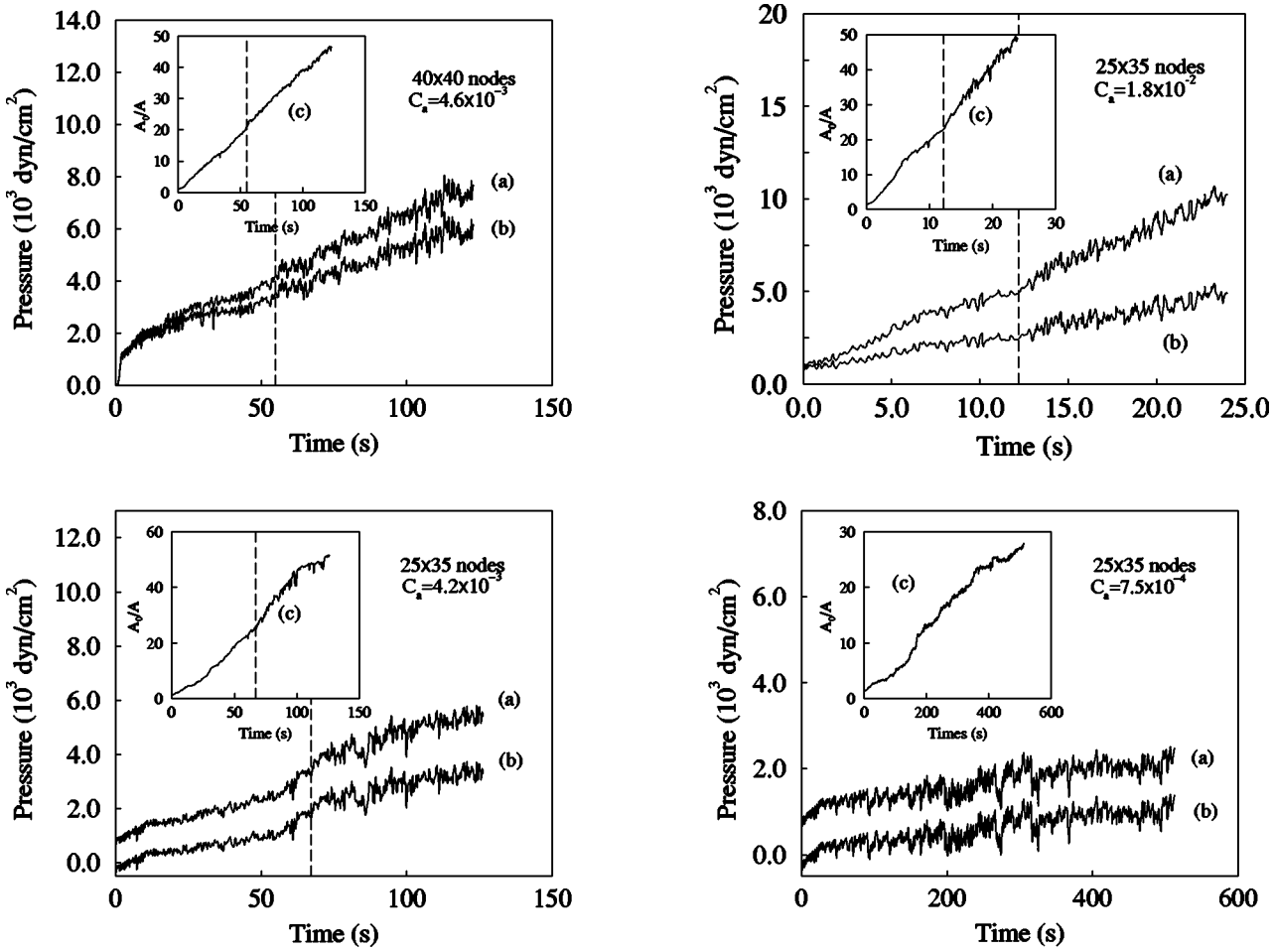

FIG. 7. ΔP (a), P_{cg} (b), and A_0/A (c) as functions of time for simulations with $M=1.0\times10^2$ at low, intermediate, and high C_a. The lattice size is given in the plot. Note that for $C_a=4.2\times10^{-3}$and 7.5×10^{-4} P_{cg} has been subtracted by 1000 dyn/cm^2 to avoid overlap of the curves. The vertical dashed lines indicate the saturation time where the front stabilizes.

those capillary forces contributes to the observed increase in P_{cg}. In the limit of high injection rate with $M<1$ (viscous fingering) few clusters develop and the extra contribution to P_{cg} from the cluster menisci becomes negligible. This is consistent with the reported observation in the preceding section, that at high injection rate when $M<1$, P_{cg} was found to fluctuate around the average threshold value for the tubes.

From Fig. 7 we also observe that at high injection rates and at large times ΔP, P_{cg}, and the difference $\Delta P-P_{cg}$ increase linearly in time. The linearity of P_{cg} is explained by again looking at the generation of the clusters in the system. All the displacements except that at $C_a=7.5\times10^{-4}$ reached the saturation time t_s where the front stabilizes. In Fig. 7 this is indicated by a vertical dashed line. Furthermore, on average every cluster contributes to P_{cg} with a certain amount making P_{cg} proportional to the number of clusters behind the front. For large times ($t>t_s$) when the front has saturated with fully developed clusters behind, the number of clusters increases linearly with the average front position h. When $t>t_s$, h itself becomes proportional to the time since the injection rate is kept constant through the displacement. In summary, we obtain

$$P_{cg}\propto h\propto t, \quad t>t_s. \tag{12}$$

It has to be emphasized that there might be large deviations from the observed linearities when clusters of size comparable to the system develop. The argument does not apply when $t<t_s$ either. Then the average shape of ΔP and P_{cg} depends on the fractal development of the displacement structure.

At $C_a=7.5\times10^{-4}$ in Fig. 7 we observe that the average increase in ΔP and P_{cg} becomes small. The low injection rate in this limit reduces the viscous drag on the clusters giving only small extra contributions to P_{cg}. Thus we approach the regime of capillary fingering where the injection rate is so low that the viscous drag becomes negligible and P_{cg} reduces to that describing the capillary fluctuations along the front.

The quantity A_0/A plotted as graph (c) in Fig. 7 is proportional to the pressure difference $\Delta P-P_{cg}$. Using Eq. (10), we obtain

$$\frac{A_0}{A}=A_0\,\frac{\Delta P-P_{cg}}{Q}, \tag{13}$$

after multiplication with A_0 on both sides of the equation. From Fig. 7 we see that A_0/A and therefore $\Delta P-P_{cg}$ is proportional to the injection time at high capillary numbers when $t>t_s$.

The quantity A in Eq. (13) has a simple interpretation and the observed linearity of $1/A$ has one important consequence. We may compare the tubes in the network to resistors with a conductivity (mobility) given by k_{ij}/μ_{eff}. A would then correspond to the total conductance of the lattice. We denote the total conductivity of the lattice σ_T in the following. Equation (5) may then be written

$$U=\sigma_T(\Delta P-P_{cg})\frac{1}{L}. \tag{14}$$

Here $U=Q/\Sigma$ is the flow velocity and $\sigma_T\equiv AL/\Sigma$. $1/A$ is therefore the total resistance of the system. Since a high viscosity fluid displaces a less viscosity fluid the total resistance increases with the amount of invading fluid in the system. The total resistance also depends on the resulting displacement structure because resistors connected in series or parallel give different resistance. However, at high injection rates when $t>t_s$ the local displacement structure becomes statistically invariant with respect to injection time. That means that the structure is fully developed with a given front width and cluster size distribution. The linearity of $1/A$ in this limit implies that this particular structure can be assigned a constant resistance per unit length. Consequently, the total resistance increases linearly with the average front position of the displacement structure. At low injection rates the front width never saturates and $1/A$ depends on the fractal development of the displacement structure.

We now want to study in more detail the pressure evolutions and relate them to the conventional effective permeability of the invading phase. If we again look at the global capillary pressure P_{cg}, it can be interpreted as a sum of the capillary pressures along the front menisci, P_{mf} and the capillary pressure of the cluster menisci, P_{mc}. Furthermore, for large times ($t>t_s$) we can write $P_{mc}=\Delta_{mc}h$ giving

$$P_{cg}=\Delta_{mc}h+P_{mf}. \tag{15}$$

Here Δ_{mc} denotes the proportionality factor between P_{cg} and h where $h_s<h<L$ is the average front position. h_s denotes the average position of the front when it saturates, that is, at $t=t_s$.

It is clear that P_{mf} is related to the simulated P_{cf}, the average capillary pressure of the front. However, due to limited statistics and system sizes we cannot quantify their relations. However, in the limit of very low injection rate the viscous drag on the clusters will vanish, giving $\Delta_{mc}\to 0$. Therefore in this limit we expect $P_{mf}\simeq P_{cg}\simeq P_{cf}$.

We can use the relation for P_{cg} in Eq. (15) to deduce a formula for the effective mobility G_{eff} of the system. We think of G_{eff} as the response of the system when we pump invading fluid into it at moderate injection rates where clusters of defending fluid are assumed immobile. This means that the invading fluid has to flow around the clusters. What we are seeking is an equation for the flow rate U, in the form of the Darcy law

$$U=G_{\text{eff}}(\Delta P-P_{mf})\frac{1}{L}. \tag{16}$$

Here the pressure gradient $(\Delta P-P_{mf})/L$ includes the contribution to the pressure from the cluster menisci (P_{mc}).

We start by inserting Eq. (15) into Eq. (14) to get

$$U=\sigma_T(\Delta P-\Delta_{mc}h-P_{mf})\frac{1}{L}. \tag{17}$$

Equation (17) can be written in Darcy form,

$$U=\frac{1}{1/\sigma_T+\Delta_{mc}h/UL}(\Delta P-P_{mf})\frac{1}{L}, \tag{18}$$

where we define the effective mobility of the system as

$$G_{\text{eff}}\equiv\frac{1}{1/\sigma_T+\Delta_{mc}h/UL}. \tag{19}$$

From the definition in Eq. (19) we see that G_{eff} is a function of the conductivity of the lattice plus an additional term $\Delta_{mc}h/UL$ which is due to the viscous drag on the clusters. Note that the U dependency in G_{eff} only indicates changes in Δ_{mc} between displacements executed at different injection rates. The behavior when the flow rate changes during a given displacement is not discussed here.

In the special case when the average front position has reached the outlet, i.e., $h=L$, only the invading phase flows through the system. Then $G_{\text{eff}}=K_e/\mu_2$ where K_e is the often measured effective permeability of the invading phase. From Eq. (19) we get when $h=L$

$$K_e=\frac{\mu_2}{1/\sigma_T+\Delta_{mc}/U}. \tag{20}$$

We note that this corresponds to the stationary case where the defending fluid is trapped and only the invading fluid of viscosity μ_2 flows through the lattice. From Eq. (20) follows directly the relation for the relative permeability k_{ri} of the invading phase, $k_{ri}=K_e/K$. Here K is the absolute permeability of the network.

To check the consistency of Eq. (19) we observe that at moderate injection rates where the clusters stay in place and keep their shapes, G_{eff} can be simulated directly by assigning zero permeability to tubes belonging to the trapped clusters. Thus the clusters will be frozen in their initial positions and in the calculations they are treated as additional boundary conditions where fluid cannot flow. Simulations show that when the clusters are frozen, the simulated conductivity σ_T in Eq. (14) adjusts itself such that it becomes similar to G_{eff} obtained from Eq. (19). G_{eff} in Eq. (19) was calculated from the simulated pressures P_{cg} and ΔP in Fig. 7.

C. Viscosity match, $M=1$

We have run 17 simulations with viscosity matched fluids ($M=1.0$) spread over six different capillary numbers. The different capillary numbers and the corresponding injection rates are listed in Table III. The lattice size was 40×60 nodes for all simulations. Due to long computation time we only did two simulations at the lowest capillary number. For all the other capillary numbers, we ran three simulations.

For all simulations ΔP and P_{cg} were calculated. Figure 8 shows P_{cg} for one of the simulations at highest, intermedi-

TABLE III. Values for the injection rate and the capillary number when $M=1.0$. The lattice is 40×60 nodes.

Runs	Injection rate (cm^3/min)	C_a
3	10	2.3×10^{-3}
3	4.0	9.2×10^{-4}
3	2.0	4.6×10^{-4}
3	1.0	2.3×10^{-4}
3	0.40	9.2×10^{-5}
2	0.20	4.6×10^{-5}

ate, and lowest capillary numbers. The front was found to stabilize at high injection rates [25], and when $t>t_s$ both P_{cg} and ΔP were found to increase linearly with time. This is consistent with the result from stable displacement. At lowest C_a we approach the capillary regime and again the pressure fluctuations are dominated by capillary fluctuations along the front. We note also that the sudden jumps in the pressure function at $C_a=4.6\times10^{-5}$ identify the bursts where the invading fluid proceeds abruptly. This corresponds to Haines jumps [27,28].

In the special case of $M=1$ the quantity A_0/A was found to be constant for all displacements independent of injection rate and displacement structure. This should be compared to the linear behavior at high injection rates reported when $M>1$ (Fig. 7). A_0/A is calculated by observing that $A_0/A=\Delta P-P_{cg}/\langle\Delta P-P_{cg}\rangle$. Here $\langle\Delta P-P_{cg}\rangle$ is the arithmetic mean of $\Delta P-P_{cg}$. Figure 9 shows the calculated A_0/A for one of the simulations at $C_a=2.3\times10^{-4}$. In the plot A_0/A is subtracted by 1 such that the resulting data fall close to zero. Similar results were found for the other capillary numbers, and for all simulations we calculated $A_0/A=1.0\pm1.0\times10^{-8}$. The noise is numerical. Thus $A=A_0=\Sigma K/\mu_1 L$ is constant through all simulations. In the electrical analog this means that the total conductance A of the lattice is constant.

The strong evidence that $A=A_0$ is constant can be deduced from simple considerations of the energy dissipation in the system. In analogy with electrical circuits, we define the total energy dissipation W in the system as

$$W=Q\Delta P. \tag{21}$$

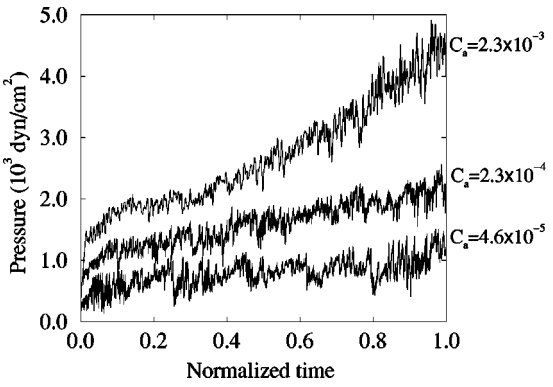

FIG. 8. P_{cg} for three simulations with $M=1.0$ at high, intermediate, and low capillary number. The injection time has been normalized to fit the data in one plot.

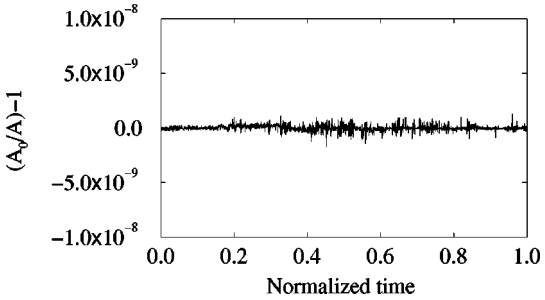

FIG. 9. A_0/A subtracted by 1 at $C_a=2.3\times10^{-3}$ and $M=1.0$. Similar results were obtained for the other capillary numbers.

The total dissipation must equal the sum of the dissipation in every tube α in the lattice. Thus

$$Q\Delta P=\sum_\alpha q_\alpha\Delta p_\alpha, \tag{22}$$

where the summation index α runs over all tubes in the lattice. q_α is given by Eq. (3) which we rewrite as $(ij\rightarrow\alpha)$

$$q_\alpha=a_\alpha\Delta p_\alpha+b_\alpha. \tag{23}$$

Here we note that a_α is proportional to $k_\alpha/\mu_{\text{eff}}$, the mobility of the tube α. By inserting Eqs. (5) and (23) into Eq. (22) we get after some reorganization

$$A\Delta P+B=\sum_\alpha a_\alpha\Delta P\left(\frac{\Delta p_\alpha}{\Delta P}\right)^2+b_\alpha\frac{\Delta p_\alpha}{\Delta P}. \tag{24}$$

By replacing the local pressure Δp_α in Eq. (24) with ΔP, using Eq. (6) we obtain after some algebra

$$Q=\left[\sum_\alpha a_\alpha\Gamma_\alpha^2\right]\Delta P+\left[\sum_\alpha \Gamma_\alpha(2a_\alpha\Pi_\alpha+b_\alpha)+\frac{\Pi_\alpha}{\Delta P}(a_\alpha\Pi_\alpha+b_\alpha)\right]. \tag{25}$$

If we compare the above equation with Eq. (5) we recognize the first summation as A and the second as B. Thus A depends entirely on a_α and Γ_α. As stated earlier, both a_α and Γ_α are proportional to the mobility of the tubes. The mobility of each tube depends on its geometry k_{ij} and the local fluid configuration, through the effective viscosity μ_{eff} [see Eq. (3)]. However, when the fluids have equal viscosities we get $\mu_{\text{eff}}=\mu_1=\mu_2$. As a consequence a_α and Γ_α become constants, which is consistent with the simulation result.

The property that $A=A_0$ is constant when the liquids have equal viscosities simplifies the computation of the nodal pressures in the lattice. By substituting A with A_0 in Eq. (5) we find that the injection rate is given by

$$Q=A_0\Delta P+B. \tag{26}$$

This equation has only one unknown, the term B, opposed to the original Eq. (5) having two unknowns, both A and B. To verify the result when A is replaced by A_0 we have compared the solution found from Eq. (26), necessitating one solution

of the flow equations, with the one given when Eq. (5) is solved twice. Not surprisingly, there is excellent agreement between these two results.

IV. DISCUSSION

We have simulated drainage displacements at different injection rates for three different viscosity ratios $M=1.0\times10^{-3}$, 1.0 and 1.0×10^{2}. The main focus of the work is the study of the temporal evolution of the pressure when a nonwetting fluid displaces a wetting fluid in porous media. Moreover, the effect of the trapped clusters on the displacement process has been discussed. From the results we clearly see that the capillary forces play an important role at both high and low injection rates.

At high injection rates with $M\geqslant1.0$ the global capillary pressure P_{cg} was found to increase as a function of the number of trapped clusters behind the front. For large times when the front has saturated, P_{cg} even became proportional to the average front position h. Using this, we derived a theory describing quantitatively the evolution of the effective mobility when the nonwetting fluid was injected into the system. Moreover, we showed that this effective mobility can be used to estimate the relative permeability of the invading phase when the average front position has reached the outlet.

At moderate injection rates the effective mobility calculated by using the behavior of P_{cg} was shown to be equivalent to assigning zero permeability to tubes belonging to the trapped clusters. When $M\ll1.0$ or at low injection rates the effect of the clusters became negligible, reducing P_{cg} to describe the local capillary fluctuations of the invading menisci along the front. With displacements performed with equal viscosities, $M=1.0$, we found that the difference $\Delta P-P_{cg}$ was constant. This was shown to be consistent with the energy dissipation in the system.

It must be emphasized that the properties we have reported are only valid for drainage. So far the model is not capable of simulating imbibition. The simulations were also performed on a two-dimensional porous system where clusters develop more easily, compared to fluid flow in three-dimensional porous media [29]. Moreover, the lattice sizes were limited by the computation time and more sophisticated and efficient algorithms have to be developed in order to increase the system sizes and thereby improve the above results. Another, and not less important exercise is to compare our simulation results with experimental measurements.

The reported correlations between the simulated pressure functions and the evolution of their fluctuation amplitudes deserve more quantitative discussions in future work. We feel that there still are many open questions to be answered and hope to supply some answers by quantitative analysis in the continuation of this project.

ACKNOWLEDGMENTS

The authors thank S. Basak, G. G. Batrouni, E. G. Flekkøy, and J. Schmittbuhl for valuable comments. The work is supported by the Norwegian Research Council (NFR) through a ''SUP'' program. We acknowledge them for a grant of computer time, and also acknowledge grants of computer time from the Idris in Paris and from HLRZ, Forschungszentrum, Jülich GmbH.

[1] K. J. Måløy, J. Feder, and T. Jøssang, Phys. Rev. Lett. **55**, 2688 (1985).
[2] J.-D. Chen and D. Wilkinson, Phys. Rev. Lett. **55**, 1892 (1985).
[3] R. Lenormand, E. Touboul, and C. Zarcone, J. Fluid Mech. **189**, 165 (1988).
[4] M. Cieplak and M. O. Robbins, Phys. Rev. Lett. **60**, 2042 (1988).
[5] M. Cieplak and M. O. Robbins, Phys. Rev. B **41**, 11 508 (1990).
[6] N. Martys, M. Cieplak, and M. O. Robbins, Phys. Rev. Lett. **66**, 1058 (1991).
[7] R. Lenormand and C. Zarcone, Phys. Rev. Lett. **54**, 2226 (1985).
[8] T. A. Witten and L. M. Sander, Phys. Rev. Lett. **47**, 1400 (1981).
[9] L. Paterson, Phys. Rev. Lett. **52**, 1621 (1984).
[10] D. Wilkinson and J. F. Willemsen, J. Phys. A **16**, 3365 (1983).
[11] J. Koplik and T. J. Lasseter, SPE J. **22**, 89 (1985).
[12] M. M. Dias and A. C. Payatakes, J. Fluid Mech. **164**, 305 (1986).
[13] P. R. King, J. Phys. A **20**, L529 (1987).
[14] M. Blunt and P. King, Phys. Rev. A **42**, 4780 (1990).
[15] M. Blunt and P. King, Transp. Porous Media **6**, 407 (1991).
[16] P. C. Reeves and M. A. Celia, Water Resour. Res. **32**, 2345 (1996).
[17] G. N. Constantinides and A. C. Payatakes, AIChE. J. **42**, 369 (1996).
[18] E. W. Pereira, W. V. Pinczewski, D. Y. C. Chan, L. Paterson, and P. E. Øren, Transp. Porous Media **24**, 167 (1996).
[19] D. H. Fenwick and M. J. Blunt, in *1997 SPE Annual Technical Conference and Exhibition* (Society of Petroleum Engineers, Inc., San Antonio, Texas, 1997).
[20] S. C. van der Marc, T. Matsuura, and J. Glas, Phys. Rev. E **56**, 5675 (1997).
[21] E. Aker, K. J. Måløy, A. Hansen, and G. G. Batrouni, Transp. Porous Media (to be published).
[22] E. W. Washburn, Phys. Rev. **17**, 273 (1921).
[23] G. G. Batrouni and A. Hansen, J. Stat. Phys. **52**, 747 (1988).
[24] R. Lenormand, C. Zarcone, and A. Sarr, J. Fluid. Mech. **135**, 337 (1983).
[25] D. Stauffer and A. Aharony, *Introduction to Percolation Theory* (Taylor & Francis, London, 1992).
[26] O. I. Frette, K. J. Måløy, J. Schmittbuhl, and A. Hansen, Phys. Rev. E **55**, 2969 (1997).
[27] W. B. Haines, J. Agric. Sci. **20**, 97 (1930).
[28] K. J. Måløy, L. Furuberg, J. Feder, and T. Jøssang, Phys. Rev. Lett. **68**, 2161 (1992).
[29] D. Wilkinson, Phys. Rev. A **34**, 1380 (1986).